The Meteoritical Society

Meteoritics & Planetary Science 49, Nr 12, 2201–2218 (2014)
doi: 10.1111/maps.12389

NanoSIMS analysis of organic carbon from the Tissint Martian meteorite: Evidence for the past existence of subsurface organic-bearing fluids on Mars

Yangting LIN[1*], Ahmed EL GORESY[2], Sen HU[1], Jianchao ZHANG[1], Philippe GILLET[3], Yuchen XU[1], Jialong HAO[1], Masaaki MIYAHARA[4], Ziyuan OUYANG[5], Eiji OHTANI[4], Lin XU[6], Wei YANG[1], Lu FENG[1], Xuchao ZHAO[1], Jing YANG[7], and Shin OZAWA[4]

[1]Key Laboratory of Earth and Planetary Physics, Institute of Geology and Geophysics, Chinese Academy of Sciences, Beijing 100029, China
[2]Bayerisches Geoinstitüt, Universität Bayreuth, 95447 Bayreuth, Germany
[3]EPFL, CH-1015, Lausanne, Switzerland
[4]Institute of Mineralogy, Petrology and Economic Geology, Graduate School of Science, Tohoku University, Sendai 980-8578, Japan
[5]Institute of Geochemistry, CAS, Guiyang, China
[6]National Astronomical Observatories, CAS, Beijing, China
[7]Guangzhou Institute of Geochemistry, CAS, Guangzhou, China
[*]Corresponding author. E-mail: linyt@mail.igcas.ac.cn

(Received 02 July 2014; revision accepted 08 October 2014)

Abstract–Two petrographic settings of carbonaceous components, mainly filling open fractures and occasionally enclosed in shock-melt veins, were found in the recently fallen Tissint Martian meteorite. The presence in shock-melt veins and the deuterium enrichments (δD up to +1183‰) of these components clearly indicate a pristine Martian origin. The carbonaceous components are kerogen-like, based on micro-Raman spectra and multielemental ratios, and were probably deposited from fluids in shock-induced fractures in the parent rock of Tissint. After precipitation of the organic matter, the rock experienced another severe shock event, producing the melt veins that encapsulated a part of the organic matter. The C isotopic compositions of the organic matter ($\delta^{13}C = -12.8$ to -33.1‰) are significantly lighter than Martian atmospheric CO_2 and carbonate, providing a tantalizing hint for a possible biotic process. Alternatively, the organic matter could be derived from carbonaceous chondrites, as insoluble organic matter from the latter has similar chemical and isotopic compositions. The presence of organic-rich fluids that infiltrated rocks near the surface of Mars has significant implications for the study of Martian paleoenvironment and perhaps to search for possible ancient biological activities on Mars.

INTRODUCTION

Mars orbital and rover missions have brought numerous lines of evidence for the past presence of water on Mars, one of the key ingredients of life. The detection of methane in the Martian atmosphere by the Mars Express orbiter (Formisano et al. 2004) has revived the search for life on Mars, although the origin of the methane is still debated (Keppler et al. 2012; Kerr 2012). The Martian rover Curiosity is equipped to detect organic compounds, including methane, and to measure their isotopic compositions (Leshin et al. 2013; Ming et al. 2014), although no organic compounds have been reported (Webster et al. 2013). Another approach is to analyze Martian meteorites, the only available rocks from Mars. However, terrestrial contamination is a critical issue especially for organic compounds, as most Martian meteorites were recovered after long residence times in Antarctic ice or hot deserts. There have been only four witnessed Martian meteorite falls, and they have also experienced ambient terrestrial conditions for more than 51 yr. Tissint is a new Martian meteorite fall (Chennaoui Aoudjehane et al. 2012), supplying us with uniquely fresh samples to

search for traces of biotic activities on Mars and to study the Martian paleoenvironment's habitability for life. Here, we report on the presence of organic carbon components in Tissint, and the in situ analyses of multiple elemental and isotopic compositions by NanoSIMS 50L. Based on both the petrographic observations and the NanoSIMS analyses, we try to clarify possible sources of these organic carbon components. Preliminary results were reported by (Lin et al. 2013a, 2013b, 2013c).

MATERIALS AND METHODS

Meteorite Sample Preparation

Tissint is the fifth witnessed fall of Martian meteorites, and many fragments were recovered from the Moroccan desert 3 months after its fall on 18 July 2011 (Chennaoui Aoudjehane et al. 2012). For this study, four slices (0.5–0.8 mm) were cut from a 6.4 g fragment of Tissint, with approximately 80% of the fragment surface covered by fresh and glazy fusion crust. Three slices were embedded in epoxy and made into normal polished sections. Another polished section was prepared from the fourth slice using Crystalbond™ mounting adhesive instead of epoxy. To eliminate any possible contamination of H and C from the adhesive, the fourth polished section was cleaned by completely dissolving the Crystalbond™ mounting adhesive in analytical reagent acetone for approximately 8 h; this cleaning process was repeated six times (for a total time of 48 h), after which the adhesive-free section was dried at 110 °C in vacuum for 48 h. This treatment does not result in any known introduction of C, H, or N into insoluble kerogen-like organic matter or isotopic exchange of these elements with either acetone or water, as soluble organic components were generally extracted from samples via refluxing organic solvents for several days, a routine treatment in organic geochemistry (Schwab et al. 2005). The adhesive-free section was pressed into an indium disk and coated with gold, and used for searching organic matter. The other three sections were carbon-coated only for petrographic observations. It was very difficult to search for organic matter in these epoxy-bearing sections, because all of the fractures were filled with epoxy that appears no different from organic matter in SEM images.

Graphite Standards and Coal Working Reference

A ½ inch round indium disk embedded with polished pieces of two types of graphite and a fragment of coal were used as standards and a working reference, respectively. The bulk C isotopic compositions of the graphite standards and the bulk C, N, and H isotopic compositions of the coal working reference were determined by measuring three aliquots of each sample with a MAT 252 type stable isotope mass spectrometer at the Stable Isotope Laboratory, Institute of Geology and Geophysics, CAS (IGG) in Beijing. About 10 mg of each aliquot mixed with 4 g of CuO was loaded in a vacuum extracting system, and heated to 780 °C for 4 h. The produced CO_2 was then purified, and then measured for $^{13}C/^{12}C$ ratios with the MAT 252. The analytical uncertainty (2 SD) is <0.2‰. Meanwhile, the water produced was reacted with 1.5 g of Cr powder at 850 °C for 16 min, producing H_2 that was measured for D/H ratios with the same MAT 252. The analytical uncertainty (2 SD) for D/H ratios is 1‰. Finally, another 10 mg of each aliquot was mixed with 3 g of CuO, 4.5 g of Cu, and 0.6 g of CaO, and was loaded in the vacuum extracting system, heated at 850 °C for 2.5 h. The produced N_2 was purified and measured for $^{15}N/^{14}N$ ratios with a Thermo Delta V advantage MS. The analytical uncertainty (2 SD) of $^{15}N/^{14}N$ ratios is 0.2‰. To confirm the C isotopic compositions of the graphite standards, three aliquots of each graphite standard were also measured for $^{13}C/^{12}C$ ratios with a GV isoprime ratio mass spectrometer (IRMS) coupled with Dual Inlet at the State Key Lab of Isotope Geochemistry, Guangzhou Institute of Geochemistry, CAS (GIG), following a method described by Jia et al. (2003). These results are summarized in Table 1. In addition, the concentrations of H, C, N, and O of the bulk graphite standards and the coal working reference have been measured, following a method described as a standard procedure for analysis of C, H, N, and O in rock organics (Li et al. 2003), with a Vario MICRO cube element analyzer at the Petroleum Geology Research and Laboratory Center in Beijing, and the results are given in Table 2.

SEM and Laser Micro-Raman Spectroscopy

The polished sections were investigated with a LEO 1450VP scanning electron microscope (SEM), equipped with a backscattered electron (BSE) detector and an energy dispersive spectrometer (EDS) at the Institute of Geology and Geophysics, Chinese Academy of Sciences. High-magnification images of the carbon grains were acquired with a field emission SEM (FE-SEM) at the School of Earth and Space Sciences, Beijing University.

Micro-Raman spectra of the carbonaceous components were obtained with a Renishaw RM-2000 type laser Raman spectrometer at the Technical Institute of Physics and Chemistry, Chinese Academy of Sciences. The Raman spectra were acquired using a laser with a wavelength of 532 nm and an output power

Table 1. Isotopic compositions of the graphite standards and the coal reference.

Samples	Reference	*n*	$\delta^{13}C_{VPDB}$	SD	$\delta^{15}N$	SD	δD	SD
Graphite-1	IGG	3	−32.90	0.05				
Graphite-1	GIG	3	−33.38	0.15				
Average			*−33.14*					
Error			*0.20*					
Graphite-2	IGG	3	−25.99	0.05				
Graphite-2	GIG	3	−25.91	0.16				
Average			*−25.95*					
Error			*0.21*					
Coal	IGG	9	−23.45	0.89	3.0	0.2	−147	1.1

SD = standard deviation of analyses; *n* = analysis number.
The bulk N and H isotopes of the graphite standards have not been measured, because of their low concentrations.

Table 2. Abundances of H, C, N, and O in the graphite standards and the coal reference.

Samples	N wt.%	C wt.%	H wt.%	O wt.%	N/C	H/C	O/C
Coal	1.66	76.28	4.25	12.53	0.0187	0.669	0.123
Coal	1.49	76.35	4.67	12.65	0.0167	0.734	0.124
Coal	1.36	75.47	4.87	13.23	0.0154	0.774	0.131
Average	*1.50*	*76.03*	*4.60*	*12.80*	*0.0169*	*0.726*	*0.126*
SD	*0.15*	*0.49*	*0.31*	*0.38*	*0.0016*	*0.053*	*0.005*
Graphite-1	0.09	98.35	0.53	0.14	0.0008	0.065	0.001
Graphite-2	0.20	96.37	0.65	0.12	0.0018	0.081	0.001

N/C, H/C, and O/C are atomic ratios. SD = standard deviation of analyses.

of 5 mW, focused on a diameter of approximately 1 μm on the surface of the sample. The spectrometer was calibrated with a single crystal silicon standard with a band peak at 520.5 cm^{-1}. The resolution of the Raman spectra is 1.7 cm^{-1}. Each analysis was acquired in the range of 1000–2000 cm^{-1} for five runs with a total integration time of 50 s. The Raman spectra were then processed with Origin software. After subtracting the linear baseline, the peak positions of both G-band and D-band and the full width at half maximum (FWHM) of the G-band were determined, using a least-squares curve fitting method and the Lorentz peak model. A constraint-free iteration option was applied to all parameters (e.g., peak position, height, and width), and the fitting calculation ended at convergence. The uncertainty of the peak positions is <2 cm^{-1}, and that of FWHM is <5 cm^{-1}, determined by repeating the curve-fitting processes three times.

NanoSIMS Analyses

The carbon grains were analyzed in situ with the Cameca NanoSIMS 50L secondary ion mass spectrometer (SIMS) at the Institute of Geology and Geophysics, Chinese Academy of Sciences in Beijing. The adhesive-free section of Tissint, the graphite standards, and the coal reference were loaded in the airlock and heated overnight, after which they were stored in the vessel chamber under high vacuum for a week before analysis. The primary beam is Cs^+, accelerated to 16 keV with a beam current of approximately 1.8 pA (approximately 100 nm in diameter) or approximately 40 pA (approximately 400 nm in diameter) for H isotope analysis. The samples were measured in four individual sets in the following sequence: (1) element mapping, (2) spot analysis of elements, (3) analysis of C and N isotopes, (4) analysis of H isotopes and H/C ratios. The isotope analyses were conducted in a sequence of standard-samples-standard, to calibrate instrumental mass fractionation (IMF). Prior to analysis, the surface of each analysis area was presputtered with a beam of 100 pA (1 nA for H isotopes) for 2 min to remove the Au coating, eliminate surface contamination, and implant Cs^+ to achieve stable secondary ion yields. An electron gun was utilized for charge compensation of the analysis area. Stability of the magnetic field was ensured through use of the nuclear magnetic resonance (NMR) mode.

Element Mapping

The instrument was configured for mapping $^{12}C^-$, $^{12}C^1H^-$ (for H), $^{16}O^-$, $^{12}C^{14}N^-$ (for N), $^{31}P^-$, $^{32}S^-$, and $^{35}Cl^-$ simultaneously, with $^{12}C^-$ as the reference. The mass resolving power (MRP) was tuned to approximately 5000 (M/ΔM, 10% definition) at ^{12}C,

sufficient to eliminate interferences of $^{12}C^{1}H^{-}$ by $^{13}C^{-}$, and $^{12}C^{14}N^{-}$ by $^{12}C_2H_2^{-}$, and $^{12}C^{13}CH^{-}$. Areas of 10×10 μm^2, larger than the carbon grains, were rastered by the primary beam (approximately 1.8 pA, approximately 100 nm) to acquire 256×256 pixel images. The dwell time was 10 ms/pixel, and each image consists of five frames with a total measurement time 1 h 8 min. After measurement, the data were corrected off-line for image shift and then added together.

Analyses of Elements

After element mapping, the carbon grains were analyzed in Spot Mode with each analysis area counted as a single point instead of an image and with the same configuration except for replacing $^{12}C^{14}N$ with ^{19}F. The primary beam was rastered over analysis areas of approximately 3×3 μm^2 within each carbon grain. Each analysis consisted of 10 blocks of 40 cycles, with a total integration time of 216 s. The secondary ion signals from the margins of 25% of the analysis area were blanked to minimize possible contamination from the surrounding areas. The results were corrected for dead-time of the electron multipliers (EMs) (44 ns) and calibrated for the relative abundances of the isotopes. The atomic O/C ratios were calibrated with a relative sensitivity factor (RSF) of 0.76, which was determined from the O/C ratio of the coal reference listed in Table 2. The analytical uncertainties are estimated at approximately 6%, mainly due to heterogeneity of the coal reference. Although the analyses of other elements were not corrected for matrix effects, their abundance ratios relative to C can be compared with the graphite standards and the coal working reference. Hydrogen was also measured in the session of H isotopes described below. We used this data set to plot, because H contamination from the surrounding surface is reduced for a higher primary beam current.

Analyses of C and N Isotopes

The instrument was reconfigured for measurements of $^{12}C^{-}$, $^{13}C^{-}$, $^{12}C^{14}N^{-}$, and $^{12}C^{15}N^{-}$. The MRP was increased to approximately 10,000, to resolve interferences of $^{13}C^{-}$ from $^{12}C^{1}H^{-}$; $^{12}C^{14}N^{-}$ from $^{12}C_2H_2^{-}$, $^{12}C^{13}CH^{-}$, and $^{13}C_2^{-}$; and $^{12}C^{15}N^{-}$ from $^{13}C^{14}N^{-}$. The primary beam (approximately 1.8 pA, approximately 100 nm) was rastered over each analysis area of 3×3 μm^2, at a rate of 0.541 s/cycle. Each analysis contains 10 blocks of 40 cycles, with a total analysis time approximately 4 min for both the samples and the standards. The raw counts were first corrected for the dead-time of the EMs. The analytical uncertainty of the raw output is the standard error.

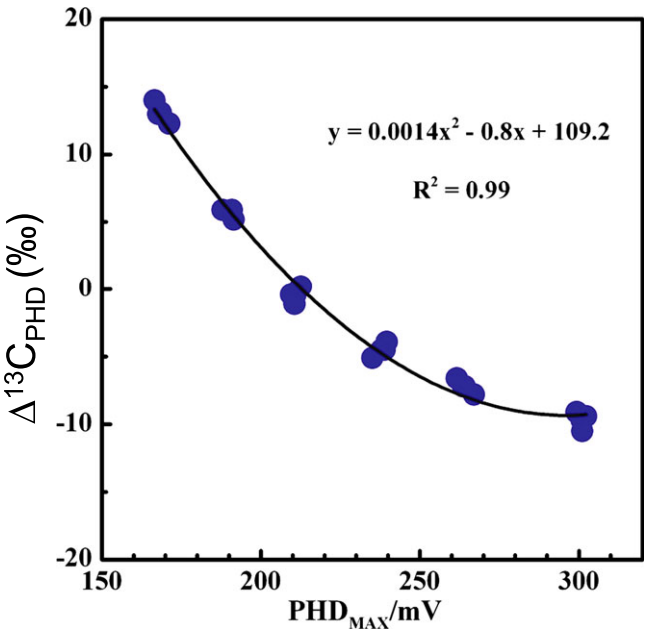

Fig. 1. The influence of pulse height distribution (PHD_{max}) on the carbon isotope ratio of the graphite-1 standard. $\delta^{13}C_{PHD} = \delta^{13}C_{raw}$-$\Delta^{13}C_{PHD}$, here $\delta^{13}C_{PHD}$ has been corrected for the aging effect, $\delta^{13}C_{raw}$ is the raw data, and $\Delta^{13}C_{PHD}$ is the relative variation due to the aging effect. This correction is rather small, <1.2‰.

The count rates of $^{12}C^{-}$ on the graphite standards were approximately 500,000 cps, causing faster aging of this EM detector than the others. To minimize differences in the EM yields, the pulse height distribution (PHD) of the EM detector of ^{12}C was measured every approximately 12 h, and the high voltage (HV) for the EM was adjusted to ensure similar maximum of the PHD. Furthermore, the analyses were calibrated for the aging effect (Slodzian 2004), using the correlation between variation in $\delta^{13}C$ (labeled as $\Delta^{13}C_{PBD}$) and PHD_{max} determined from the graphite-1 standard by manually changing the HV (Fig. 1). The PHD_{max} of each analysis was interpolated with the total counts accumulated. This correction is rather small within two adjustments of the HV of EM, <1.2‰, and the uncertainty of the correction is <0.1‰ and is ignored.

After correction for dead-time and aging, the analyses were calibrated for the quasi-simultaneous arrival (QSA) effect (Slodzian et al. 2004; Zhang et al. 2014), using the equation: $R_{meas} = R_{true} \times (1 + \beta \times K)$. Here, K is the average number of secondary ions ejected per primary ion, β is the experimental coefficient. The primary beam current on the samples (Fco) was determined from the primary column current (Fcp), which was monitored before and after each analysis. The parameter β was approximately 0.816, determined

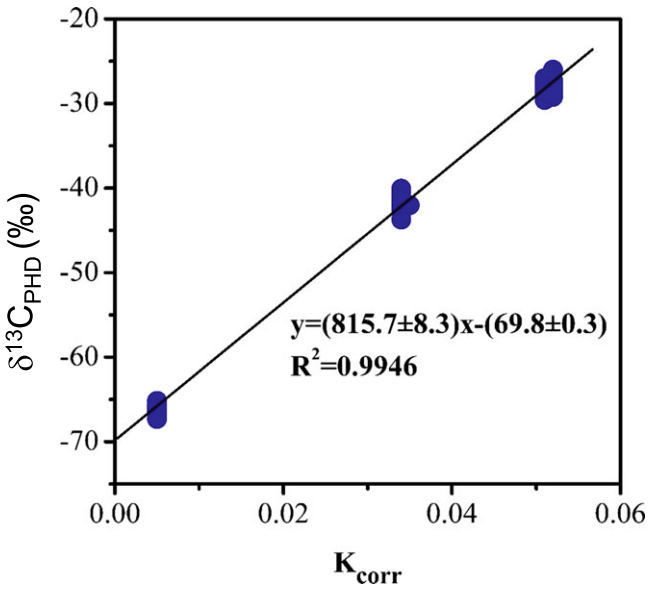

Fig. 2. QSA effect on $\delta^{13}C$ values. The correlation between the measured $\delta^{13}C_{PHD}$ and parameter K_{corr} was determined from the graphite-1 standard by changing the aperture slits. $\delta^{13}C_{QSA} = \delta^{13}C_{PHD} = -69.8 \pm 0.3‰$, at $K_{corr} = 0$. Hence, $\delta^{13}C_{QSA} = \delta^{13}C_{PHD} - (0.816 \pm 0.008) \times K_{corr} \times 1000‰$.

from the graphite-1 standard by changing the aperture slits (Fig. 2). The variation of $\delta^{13}C$ can be determined as: $\delta^{13}C_{PHD}$-$\delta^{13}C_{QSA} = (0.816 \pm 0.008) \times K_{corr} \times 1000‰$, here $\delta^{13}C_{QSA}$ is the QSA-corrected value at $K_{corr} = 0$. The correction for QSA effect is up to −37.5‰, but the relative variations between the graphite standard and the samples are <16.3‰. The uncertainty of the QSA correction is approximately 1‰ (Zhang et al. 2014).

Finally, the results were corrected for instrumental mass fractionation (IMF) determined from the graphite-1 standard. The results were expressed as $\delta^{13}C_{VPDB} = ([^{13}C/^{12}C]_{sample}/[^{13}C/^{12}C]_{VPDB} - 1) \times 1000‰$, here $(^{13}C/^{12}C)_{VPDB} = 0.0112372$. To assess all corrections for PHD, QSA, and matrix effects, and the precisions of the analyses, the graphite-2 standard and the coal working reference were measured as unknown samples, calibrated by the graphite-1 standard. The results are summarized in Table 3. It is demonstrated that the NanoSIMS results (1 SD) (graphite-2: $\delta^{13}C = -25.2 \pm 3.8‰$, coal: $-26.4 \pm 1.4‰$) are similar, within the analytical uncertainties, to the values determined by stable mass spectrometry (graphite-2: $\delta^{13}C = -25.95 \pm 0.16‰$, coal: -23.45 ± 0.89). The total analytical error includes counting uncertainty and correction errors for QSA and IMF. For N isotopes and N/C ratios, the IMF and RSF were determined from the coal reference, and are $-2.1 \pm 5.6‰$ and 0.13, respectively. However, the analytical errors for $\delta^{15}N$ and N/C ratios cannot be assessed from analyses of the graphite standards that are highly depleted in N. The heterogeneities of the coal working reference (1 SD), 5.6‰ for $\delta^{15}N$, and 6% for N/C ratio, or the counting uncertainties of the samples, whichever are the larger ones, could be referred to as the analytical errors.

Analyses of H Isotopes and H/C Ratios

A high vacuum condition is required for analyses of H isotopes and H/C ratios; in this study, the vacuum was better than 3×10^{-10} torr in the analysis chamber during these measurements. The H background was monitored by analyzing San Carlos olivine standard, and was <10 ppm. The instrument was configured to measure $^1H^-$, $^2D^-$, and $^{13}C^-$, with a MRP of approximately 3000 at $^1H^-$. Prior to measurement, each analysis area was presputtered with a high primary beam current (approximately 1 nA) to effectively remove surface contamination and achieve a stable yield rate of the secondary ions. In this analytical session, we used a high primary beam current (approximately 40 pA) rastered over the analysis areas. The secondary ion signals from the margins of 25% of the analysis area were blanked, to minimize H from the surrounding areas. Each analysis consisted of 5 blocks of 100 cycles, with a total analysis time of approximately 5 min. The results are given as $\delta D_{SMOW} = ((D/H)_{sample}/(D/H)_{SMOW} - 1) \times 1000‰$. The coal working reference has an average δD value of $-147 \pm 1‰$ determined with the stable mass spectrometer, and the IMF is +126‰. The H/C ratios were calibrated using a RSF of 6.7, determined from the coal reference.

RESULTS

Petrographic Settings

The Tissint Martian meteorite is an olivine-phyric basalt, consisting mainly of olivine phenocrysts in a more fine-grained pyroxene-maskelynite (shocked plagioclase glass) matrix, with minor chromite, ilmenite, pyrrhotite, and phosphates (Chennaoui Aoudjehane et al. 2012; Irving et al. 2012; Lin et al. 2012; El Goresy et al. 2013b). The Tissint whole rock has low rare earth element (REEs) abundances with a significantly LREE-depleted pattern, similar to other depleted Martian basalts. However, a LREE-enriched composition was also reported in black glass (probably the shock-melt veins and/or pockets), which was interpreted as the presence of a near-surface Martian component (Chennaoui Aoudjehane et al. 2012). Tissint has been heavily shocked, producing shock-melt veins and pockets and abundant fractures. It probably experienced multiple shock events (El Goresy et al. 2013b).

Table 3. Measurements of C isotopes of the graphite-2 standard and the coal working reference, with graphite-1 as the standard.

Sample ID	K_{corr}	$\delta^{13}C_{raw}$	SE	$\delta^{13}C_{PHD}$	$\delta^{13}C_{QSA}$	$\delta^{13}C$	SE*	IMF
Graphite-1a	0.042	−39.9	1.1	−39.2	−73.5	−35.9	3.5	
Graphite-1a	0.041	−37.8	1.1	−37.1	−70.6	−33.0	3.5	
Graphite-1a	0.040	−38.1	1.1	−37.3	−69.9	−32.4	3.5	
Graphite-1a	0.041	−37.6	1.2	−36.7	−70.2	−32.6	3.6	
Graphite-1a	0.041	−36.8	1.2	−35.8	−69.3	−31.7	3.6	
Average					*−70.7*	*−33.1*		*−37.5*
SD					*1.6*	*1.6*		
Graphite-2a	0.034	−34.0	1.2	−33.0	−60.7	−23.2	3.6	−37.5
Graphite-2a	0.035	−37.1	1.3	−36.1	−64.7	−27.1	3.6	−37.5
Graphite-2a	0.033	−35.4	1.2	−34.3	−61.2	−23.7	3.5	−37.5
Graphite-2a	0.038	−38.4	1.3	−37.2	−68.2	−30.7	3.6	−37.5
Graphite-2a	0.035	−31.3	1.3	−30.1	−58.7	−21.1	3.6	−37.5
Average					*−62.7*	*−25.2*		
SD					*3.8*	*3.8*		
Graphite-1b	0.042	−24.6	1.5	−24.7	−59.0	−32.5	3.6	
Graphite-1b	0.040	−28.4	1.4	−28.5	−61.1	−34.7	3.6	
Graphite-1b	0.040	−26.8	1.3	−26.9	−59.5	−33.1	3.5	
Graphite-1b	0.041	−25.3	1.6	−25.4	−58.9	−32.4	3.6	
Average					*−59.6*	*−33.1*		*−26.5*
SD					*1.1*	*1.1*		
Coal	0.024	−32.5	2.1	−32.6	−52.2	−25.7	4.3	−26.5
Coal	0.024	−34.0	2.2	−34.1	−53.7	−27.2	4.4	−26.5
Coal	0.023	−32.0	2.2	−32.0	−50.8	−24.3	4.4	−26.5
Coal	0.024	−34.4	2.1	−34.4	−54.0	−27.5	3.3	−26.5
Coal	0.024	−34.8	2.0	−34.9	−54.5	−28.0	3.3	−26.5
Coal	0.023	−33.6	2.4	−33.6	−52.4	−25.9	3.6	−26.5
Average					*−52.9*	*−26.4*		
SD					*1.4*	*1.4*		

K_{corr} = the secondary ions ejected per primary ion.
$\delta^{13}C_{Raw}$ = raw data; $\delta^{13}C_{PHD}$ = PHD_{max} corrected; $\delta^{13}C_{QSA}$ = QSA corrected using parameter K_{corr}.
$\delta^{13}C_{QSA} = \delta^{13}C_{PHD} - (0.816 \times K_{corr}) \times 1000‰$.
$\delta^{13}C$ = final correction for IMF, with $\delta^{13}C_{true} \approx \delta^{13}C_{QSA}$-IMF. The measurements were carried out in two separate sessions with different IMF values.
$\delta^{13}C = ((^{13}C/^{12}C)_{sample}/(^{13}C/^{12}C)_{VPDB} - 1) \times 1000‰$, here $(^{13}C/^{12}C)_{VPDB} = 0.0112372$.
SE* = The combined analytical error includes counting uncertainty and correction uncertainties of PHD, QSA, and IMF.

Two distinct petrographic settings of carbonaceous grains were found in the adhesive-free section of Tissint studied here. Most carbonaceous matter occurs as fine veins (<10 μm wide) fully filling fractures and cleavages in olivine and pyroxene, but not in maskelynite (Fig. 3a). These fractures and cleavages terminate at the boundaries of maskelynite (Fig. 3a), a typical shock feature reported in shergottites (El Goresy et al. 2013a). FE-SEM images of the carbonaceous matter show that it consists of submicron-sized grains (Fig. 3b). In addition, a few carbonaceous aggregates with sizes up to 6 μm were found as inclusions entrained in the shock-melt veins (Figs. 3c and 3d). These also consist of submicron-sized grains similar to those filling the fractures and cleavages. Such carbonaceous inclusions have also been reported in shock-melt veins in other heavily shocked Martian meteorites (e.g., NWA 6162 and NWA 856) associated with shock-induced high-pressure phases (El Goresy et al. 2013b).

Laser Micro-Raman Spectra

The two types of carbonaceous matter were analyzed with laser micro-Raman spectroscopy. The Raman spectra exhibit a broad G-band centered at 1580 cm^{-1} and a smaller D-band at 1346 cm^{-1} (Fig. 4a), similar to those reported for kerogen (Wopenka and Pasteris 1993) and clearly distinct from those of ordered graphite. The kerogen-like carbon grains entrained in the shock-melt veins have the same Raman spectra as those filling the fracture space, except for the presence of a sharp band at 1327 cm^{-1}, characteristic of the diamond T_{2G} mode and distinguished from the D-band at 1331 cm^{-1} of the synthetic diamond used to polish the sections. This

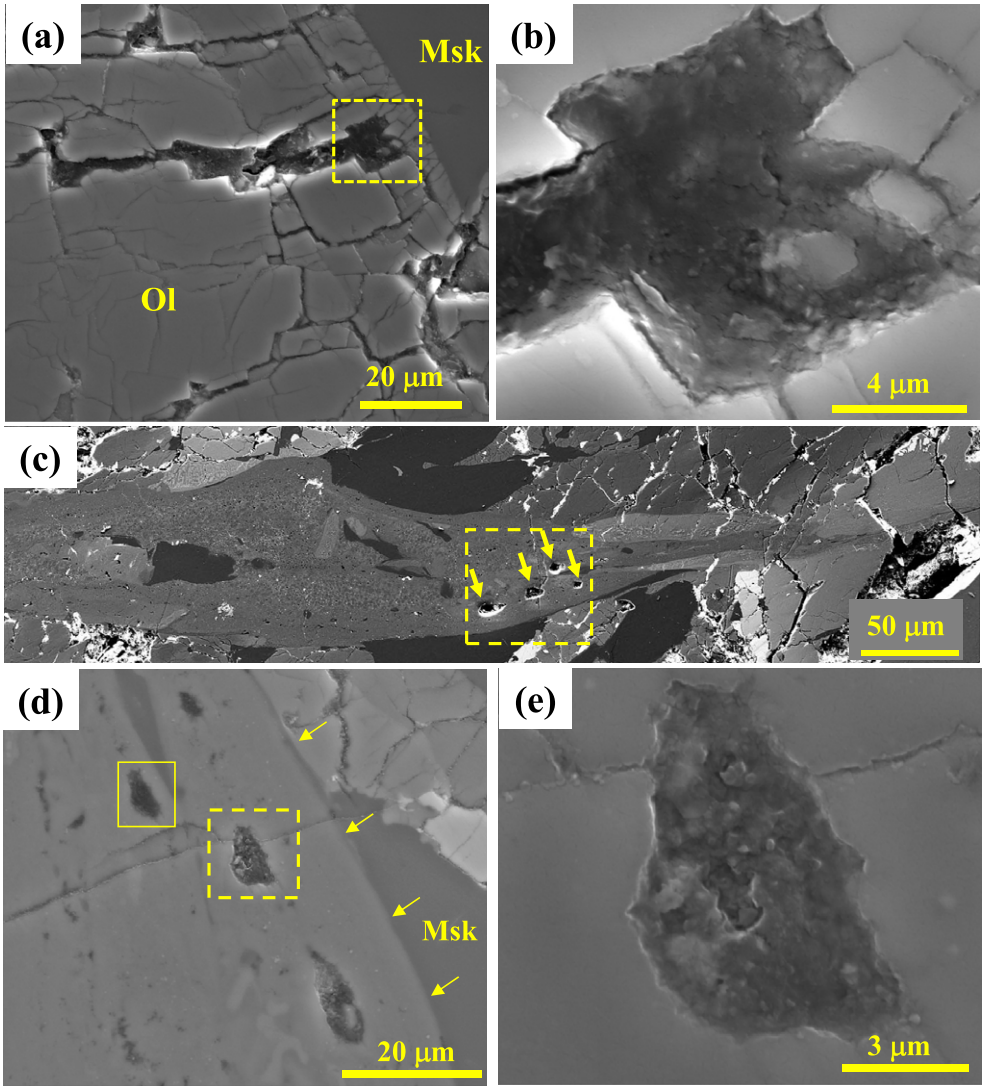

Fig. 3. SEM images of the carbonaceous matter in Tissint. a) Dark carbonaceous matter fills all of the fractures and cleavages in olivine (Ol) that terminated at the rims of maskelynite (Msk), scale bar of 20 μm; b) high magnification of the inset in (a), scale bar of 4 μm; c) dark carbonaceous inclusions (arrows) in a shock-melt vein at low magnification, scale bar is 50 μm. d) High magnification of the inset in (c) rotated approximately 90° counterclockwise. Other dark submicron-sized grains are also carbonaceous matter. The arrows point to the boundary between the shock-melt vein (left) and the host rock (right). Scale bar of 20 μm; e) high magnification of the inset in (d), note the submicron-sized grains in the inclusion. Scale bar is 4 μm.

indicates a transformation of kerogen-like carbon to diamond at high pressure by a shock event and confirms independent observations in other samples of Tissint as well as in NWA 6162 and NWA 856 (El Goresy et al. 2013b).

The positions and full widths at half maxima (FWHM) of the G-band peaks (Fig. 4b) plot within the lower range of reduced organic carbon recently described in other Martian meteorites (Steele et al. 2012). The lower FWHM values from Tissint compared with those from other Martian meteorites suggest that the carbonaceous matter in Tissint experienced a mild thermal metamorphic event (Wopenka and Pasteris 1993). Hence, the major carbonaceous components can be referred to as kerogen-like organic matter based on their Raman spectra.

Ion Imaging

Elemental distributions of C, H (as $^{12}C^{1}H^{-}$), N (as $^{12}C^{14}N^{-}$), O, P, S, and Cl were mapped in the two types of organic carbon. Figures 5 and 6 show representative organic carbon grains filling cracks and entrained in the shock-melt vein, respectively. The two petrographic settings exhibit no significant differences, except for hotspots of S in the shock-melt vein that

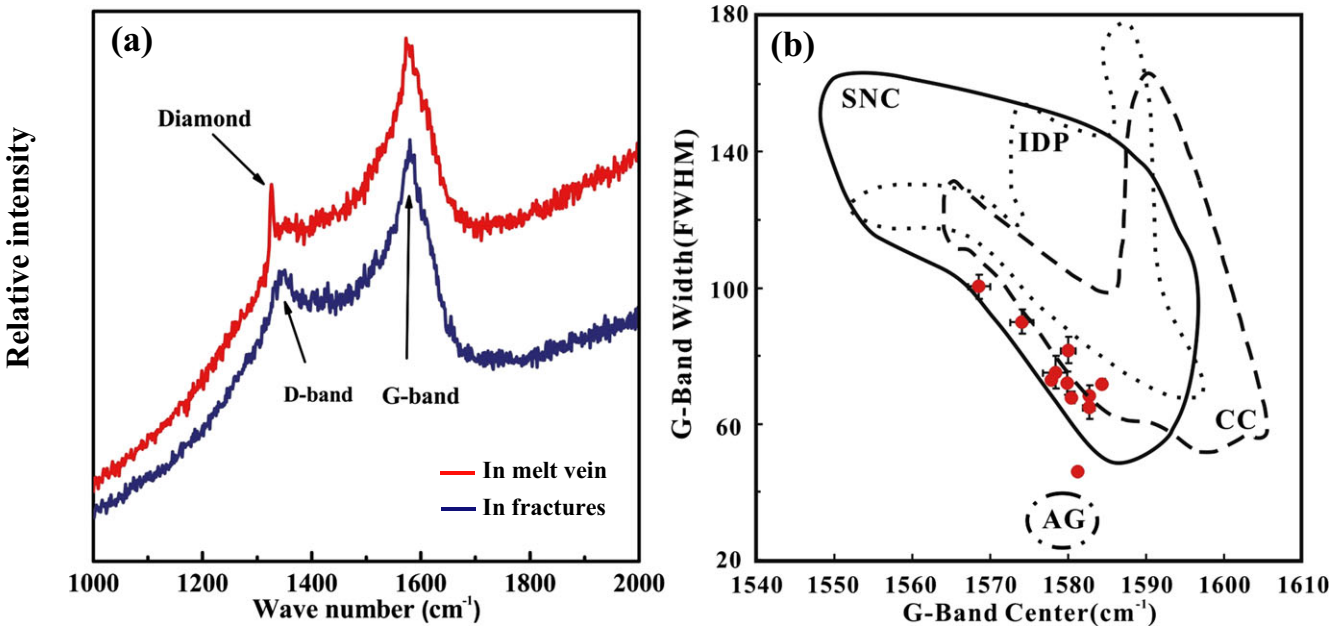

Fig. 4. Raman spectra of the carbonaceous matter in Tissint. a) Representative Raman spectra of the carbonaceous matter in the fractures (blue) and the shock-melt veins (red). Note the sharp band at 1327 cm^{-1} indicative of the T_{2G} diamond band in the carbonaceous inclusion in the melt vein; b) G-band width (FWHM) versus G-band position of the carbonaceous matter, in comparison with organic matter in other Martian basalts (SNC, solid line), carbonaceous chondrites (CC, dashed line), and interplanetary dust particles (IDPs, dotted line) and graphite (AG) (Steele et al. 2012). The error bars are the standard deviations (1 SD) of the curve fitting results repeated three times.

entrained the organic carbon inclusion, which are probably due to presence of fine-grained sulfides. Consistent with the fine grain size of the organic matter, some heterogeneity in the distributions of the elements is recognized (Figs. 6 and 7), although topographic effects on the images cannot be entirely excluded. Note, moreover, that the ion images unambiguously show that organic carbon fills the very thin cleavage fractures in the olivine (Fig. 5).

Elemental Ratios

Abundances of H, C, N, O, Cl, F, S, and P in the organic matter are given in ratios relative to C (Fig. 7; Tables 4–6). The H/C and N/C ratios were measured in different analysis sessions. In addition, only the H/C, N/C, and O/C ratios have been calibrated with relative sensitivity factors (RSFs) determined from the coal working reference, whereas other ratios were not corrected for matrix effects. The ratios of H/C, N/C, O/C, and S/C in the organic matter demonstrate more similarities to the coal working reference than the graphite standards (Fig. 7, Tables 4–6). In addition, the H/C, N/C, and O/C ratios of the organic matter also overlap the ranges of IOM from carbonaceous chondrites (Figs. 7a and 7b), providing further evidence that the carbonaceous grains are kerogen-like organic matter rather than graphite. The organic matter is also P-, F-, and Cl-rich compared with the coal working reference. This is consistent with the S-, halogen-enrichment of Martian soils measured by Mars rovers (Squyres et al. 2004; Osterloo et al. 2008; Schmidt et al. 2008; Hecht et al. 2009).

Based on confocal Raman spectroscopic data obtained on macromolecular carbon (MMC) grains, Steele et al. (2012) showed that G-band peak shapes on the whole are indicative of amorphous to poorly ordered graphitic carbon in the range recorded for carbonaceous chondrites and IDPs. Our multielemental abundance ratios relative to carbon (Fig. 7) also demonstrate a clear distinction between graphite and organic carbon, providing the extra dimensions needed to resolve MMC from graphite.

Isotopic Compositions of C, N, and H

All analyses of the C and N isotopes of the organic matter are summarized in Table 5. The $\delta^{13}C$ values of the organic matter are rather negative, with $\delta^{13}C$ ranging from −12.8‰ to −33.1‰ with an average of −20.7 ± 5.3 (1 SD). The N isotopes are normal relative to terrestrial materials, with an average $\delta^{15}N$ of 4.4 ± 8.4‰ and a range from −12.0 to 17.3‰.

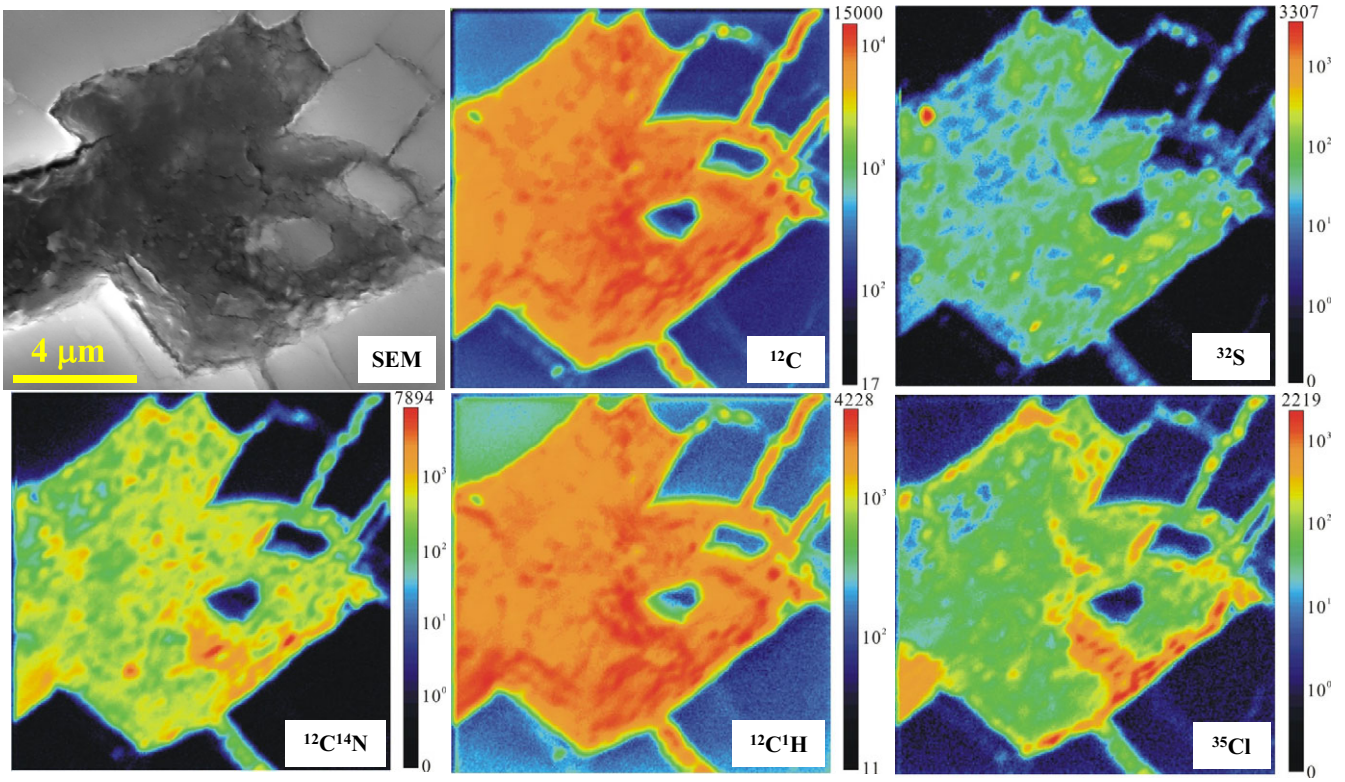

Fig. 5. NanoSIMS element images of the organic matter filling fractures. Note the heterogeneous distributions of the elements and the presence of carbon in the fine cleavage space. The relative concentrations of elements are scaled to the color intensity columns (cps) of the secondary ions. FE-SEM image is shown for comparison.

The δD values of the organic matter are summarized in Table 6. Most of the organic carbon grains are D-enriched, with δD varying from +324‰ up to +1183‰ except for 4 analyses (−51 to +7‰). No correlation between the δD values and the H/C ratios was found.

DISCUSSION

Martian Origin of the Organic Carbon

Terrestrial contamination complicates correct recognition of pristine Martian organic compounds, especially soluble organic molecules in Martian meteorite finds. Hence, the Tissint meteorite fall provides a unique opportunity for the study of Martian organic matter.

We assert that the organic matter we found in Tissint is pristine and is not terrestrial contamination. We have confirmed this by the following lines of evidence: (1) it is deuterium-enriched (up to +1183‰), a stark diagnostic feature distinguishing Martian materials from terrestrial contamination (Watson et al. 1994). Terrestrial organic matter typically has negative δD values (e.g., −20‰ ~ −150‰) (Hoefs 2009); (2) the presence of organic matter inclusions in shock-melt veins indicates its formation before production of the veins by shock events on Mars, another robust line of evidence against terrestrial contamination; (3) partial conversion of the organic carbon inclusions entrained in the shock-melt veins to diamond also points to strong impact events, which must have occurred on Mars; (4) the lower G-band width relative to MMC in other Martian meteorites, carbonaceous chondrites, and IDPs (Fig. 4b) indicates a mild thermal metamorphic event, which would not be expected for contamination in a hot desert environment; (5) the organic matter present in Tissint is insoluble in both water and acetone. It is unlikely that local organic matter in the Moroccan desert could have been deposited in interior fractures of the meteorite within a few months after its fall.

Deposition from Subsurface Organic-Rich Fluids

The carbon-filled fractures are texturally analogous to graphite deposited from fluids in terrestrial rocks, following the simplified chemical reaction CO_2+CH_4 = 2C (graphite) + $2H_2O$ (Lepland et al. 2010). However, the Raman spectra and chemical compositions of the carbon convincingly reveal that it is kerogen-like organic

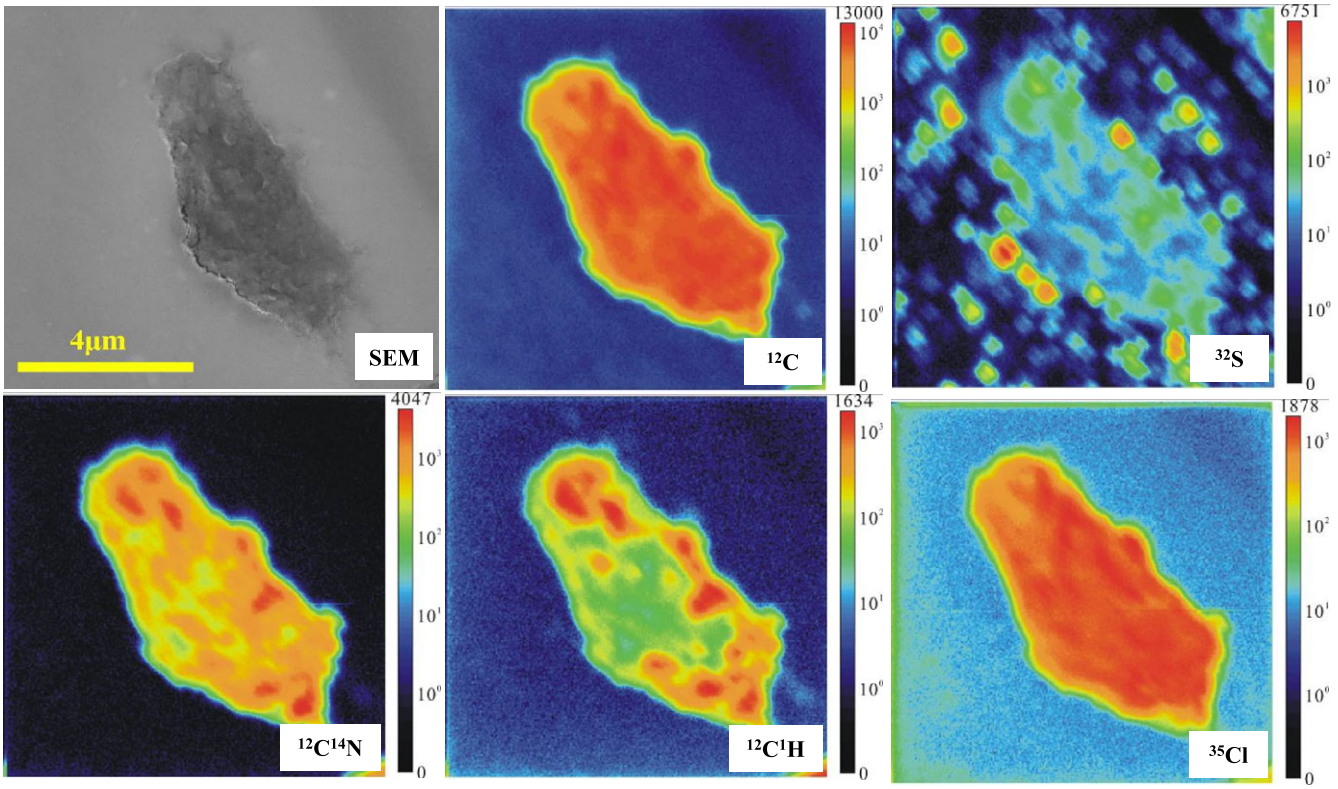

Fig. 6. NanoSIMS element images of the organic matter entrained in shock-melt veins. Elemental distributions are similar to those filling fractures. Hotspots of S in the shock-melt vein are due to the presence of pyrrhotite grains. The relative concentrations of elements are scaled to the color intensity columns (cps) of the secondary ions. FE-SEM image is shown for comparison.

in nature instead of being graphite that contains nearly pure C. Because of its insoluble nature, we propose that the organic matter was probably transferred in the form of colloid in the fluid.

We propose the following formational scenario. (1) Emplacement of the igneous basaltic host rock of Tissint near the surface of Mars. (2) After solidification and a period of residence near the surface of Mars, the igneous rock was impacted by an asteroid, highly fracturing the rock and converting plagioclase to maskelynite. Although these fractures could also be produced by other mechanisms, they would have been expected to insert or pass through adjacent maskelynite grains. In contrast, the organic-filling cleavage and fractures terminate at maskelynite (Fig. 3a). Termination of fractures in surrounding olivine and pyroxene at maskelynite is a typical shock-induced feature in shergottites (El Goresy et al. 2013a). (3) Sometime after this impact event, the Tissint host rock was infiltrated by organic-rich fluids that led to the deposition of organic matter in the shock-induced fractures and cleavages. We found no evidence for aqueous reaction of olivine in the sections, suggesting a short residence time for the organic-rich fluid in the Tissint host rock. The high concentrations of halogens and S in the organic matter suggest that the fluid was rich in S, Cl, and F, which could be derived from dissolvable sulfates, chlorides, and perchlorate detected in Martian soils (Squyres et al. 2004; Campbell et al. 2008; Osterloo et al. 2008; Hecht et al. 2009; Ming et al. 2014). (4) Following deposition of the organic matter in fracture spaces, another impact partially melted the organic-bearing host rock and produced the shock-melt veins with organic carbon inclusions. The presence of these inclusions in the shock-melt veins sets a clear lower limit for the formation time of the organic carbon. This asteroid impact also led to the formation of the diamond observed in some of the organic carbon inclusions.

Abiogenic Origins of the Organic Matter

There are basically two major abiogenic possible pathways to produce organic matter like that observed here: (1) igneous origin from the Martian mantle, via Fischer–Tropsch-Type (FTT) reactions; (2) exogenous delivery of carbonaceous chondrites and interplanetary dust particles (IDPs) to the surface of Mars.

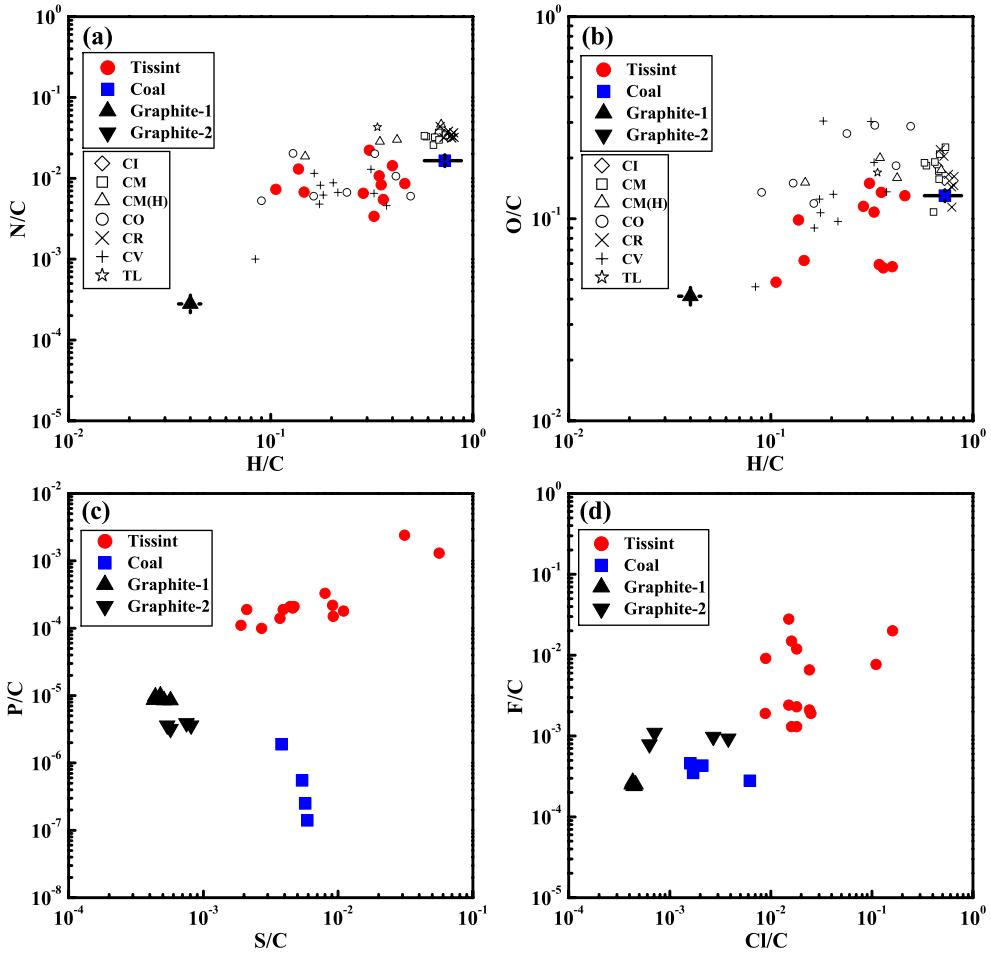

Fig. 7. Atomic ratios of elements of the organic matter. The chemical compositions of the organic matter (Tissint) are comparable to the coal reference (coal), but are largely distinct from the graphite standards (graphite-1, -2). Also note the higher abundances of P and halogens in the organic matter. Analytical uncertainties are comparable to the sizes of the symbols. Error bars for Graphite-1 and the coal reference reflect heterogeneities in the samples. Carbon in Tissint is similar to bulk IOM from CV, CO, and CM (H) (heated) groups and the ungrouped Tagish Lake (TL) carbonaceous chondrite, but is distinct from that of CM, CR, and CI groups. Literature data for carbonaceous chondrites are from Alexander et al. (2007).

An igneous origin from the Martian mantle has been inferred for macromolecular carbon (MMC) phases in Tissint and ten other Martian meteorites by Steele et al. (2012). As shown in Fig. 4b, the G-band width and position of the organic matter we observed in Tissint plot within the ranges of the MMC phases, suggestive of a similar kerogen-like organic carbon component. The MMC phases were identified beneath the surface of the sections with confocal Raman imaging spectroscopy. Steele et al. (2012) argued that this organic matter crystallized from the magmas from which these meteorites formed, due to its presence in melt inclusions within olivine and pyroxene host minerals. However, the organic matter we observed in Tissint, filling fractures, cannot be explained by this mechanism, but instead, based on petrographic considerations, was probably deposited from an organic-bearing fluid as discussed above.

An igneous origin for the carbon in Martian meteorites has also been suggested based on the results of bulk stepped combustion analyses (Grady et al. 2004; Chennaoui Aoudjehane et al. 2012). A low-temperature fraction released between 200 and 600 °C by stepped combustion of bulk Martian meteorite samples was interpreted as terrestrial contamination, whereas a high-temperature fraction released between 600 and 1000 °C was referred to as magmatic in origin (Grady et al. 2004; Chennaoui Aoudjehane et al. 2012). However, this interpretation of stepped combustion of bulk Martian meteorites without petrographic context is not unique and could have alternative explanations. We expect that the organic matter filling the open fractures will be released at low temperature (e.g., 200–600 °C), whereas that entrained in the shock-melt veins will be released at high temperature (800–1000 °C) together

Table 4. Atomic ratios of the organic matter (except for N/C ratio shown in Table 5 and H/C ratio in Table 6).

Sample ID	O/C[a]	F/C	SE	P/C	SE	S/C	SE	Cl/C	SE
58C3	4.9E-2	9.1E-3	2.3E-5	1.4E-4	1.2E-6	3.7E-3	6.2E-5	8.9E-3	1.5E-5
55C2a	1.1E-1	2.8E-2	4.1E-4	1.0E-4	1.0E-6	2.7E-3	1.9E-5	1.5E-2	1.3E-4
55C3	1.2E-1	1.5E-2	2.8E-4	2.1E-4	1.5E-6	4.4E-3	1.7E-5	1.6E-2	1.3E-4
55C4	4.9E-2	1.3E-3	4.9E-6	2.1E-4	1.4E-6	4.7E-3	1.7E-5	1.6E-2	4.8E-5
55C1	5.8E-2	1.2E-2	1.0E-4	3.3E-4	2.1E-6	8.0E-3	3.7E-5	1.8E-2	2.8E-5
58C4	5.9E-2	6.6E-3	1.3E-5	2.0E-4	1.6E-6	4.6E-3	9.5E-6	2.4E-2	3.1E-5
58C5	1.3E-1	2.3E-3	5.7E-6	1.8E-4	1.7E-6	1.1E-2	3.1E-5	1.8E-2	1.9E-5
58C1	5.7E-2	2.4E-3	1.1E-5	1.1E-4	1.0E-6	1.9E-3	4.1E-6	1.5E-2	1.4E-5
58C7	9.9E-2	1.9E-3	3.4E-5	1.9E-4	2.2E-6	2.1E-3	1.2E-5	8.8E-3	5.7E-5
58C6	1.3E-1	1.3E-3	6.5E-6	1.5E-4	1.6E-6	9.2E-3	3.7E-5	1.8E-2	2.5E-5
58C2	1.5E-1	2.1E-3	1.5E-5	2.2E-4	1.7E-6	9.1E-3	1.4E-4	2.4E-2	1.4E-4
56Cb	6.2E-2	1.9E-3	2.0E-5	1.9E-4	1.6E-6	3.9E-3	7.1E-6	2.5E-2	2.3E-5
57C1	4.5E-1	2.0E-2	8.6E-5	1.3E-3	8.0E-6	5.6E-2	3.4E-4	1.6E-1	1.9E-3
57C2	4.9E-1	7.7E-3	4.5E-5	2.4E-3	1.9E-5	3.1E-2	1.5E-4	1.1E-1	4.6E-4
Average	*1.4E-1*	*8.0E-3*		*4.2E-4*		*1.1E-2*		*3.4E-2*	
SD	*1.4E-1*	*8.2E-3*		*6.4E-4*		*1.5E-2*		*4.4E-2*	
Coal	1.3E-1	3.5E-4	5.2E-6	1.4E-7	1.0E-7	5.9E-3	2.2E-5	1.7E-3	2.4E-6
Coal	1.2E-1	2.8E-4	4.2E-6	2.5E-7	1.1E-7	5.7E-3	2.1E-5	6.2E-3	4.5E-6
Coal	1.2E-1	4.3E-4	4.6E-6	1.9E-6	2.9E-7	3.8E-3	1.4E-5	2.1E-3	2.2E-6
Coal	1.3E-1	4.6E-4	5.3E-6	5.5E-7	1.7E-7	5.4E-3	1.8E-5	1.6E-3	2.2E-6
Average	*1.3E-1*	*3.8E-4*		*7.1E-7*		*5.2E-3*		*2.9E-3*	
SD	*7.2E-3*	*7.8E-5*		*8.0E-7*		*9.4E-4*		*2.2E-3*	
Graphite-1	4.2E-2	2.5E-4	2.1E-6	1.0E-5	3.3E-7	4.8E-4	2.3E-6	4.6E-4	5.1E-7
Graphite-1	4.1E-2	2.4E-4	1.8E-6	8.5E-6	3.1E-7	5.1E-4	2.3E-6	4.4E-4	5.3E-7
Graphite-1	4.1E-2	2.5E-4	1.8E-6	9.7E-6	3.2E-7	4.4E-4	2.1E-6	4.2E-4	4.9E-7
Graphite-1	4.1E-2	2.7E-4	2.0E-6	8.6E-6	3.1E-7	4.3E-4	2.0E-6	4.3E-4	4.9E-7
Graphite-1	4.1E-2	2.4E-4	1.9E-6	8.5E-6	2.9E-7	5.7E-4	2.6E-6	4.5E-4	5.1E-7
Average	*4.1E-2*	*2.5E-4*		*9.2E-6*		*4.9E-4*		*4.4E-4*	
SD	*3.3E-4*	*1.5E-5*		*8.7E-7*		*5.6E-5*		*1.6E-5*	
Graphite-2	3.0E-2	7.9E-4	5.8E-6	3.2E-6	2.2E-7	5.7E-4	2.9E-6	6.3E-4	3.4E-6
Graphite-2	2.9E-2	1.1E-3	9.4E-6	3.6E-6	2.1E-7	5.4E-4	2.9E-6	7.1E-4	3.6E-6
Graphite-2	3.0E-2	9.8E-4	9.4E-6	3.6E-6	2.3E-7	8.1E-4	3.5E-6	2.7E-3	7.3E-6
Graphite-2	3.0E-2	9.3E-4	9.0E-6	3.9E-6	2.3E-7	7.5E-4	3.6E-6	3.8E-3	8.9E-6
Average	*3.0E-2*	*9.5E-4*		*3.6E-6*		*6.7E-4*		*2.0E-3*	
SD	*5.1E-4*	*1.3E-4*		*2.7E-7*		*1.3E-4*		*1.5E-3*	

[a]Calibrated with a relative sensitivity factor (RSF) of 0.76 determined from the coal working reference, and the analytical uncertainties are dominated by heterogeneity of the reference (approximately 6%).

Other atomic ratios have not been corrected for matrix effects, and the standard error (SE) is statistical uncertainty; SD = standard deviation of analyses.

with Martian atmospheric components encapsulated in the shock-induced glass.

Although organic compounds can also be synthesized in laboratories (Foustoukos and Seyfried 2004; McCollom et al. 2010) and produced in hydrothermal systems (Lollar et al. 2008; Proskurowski et al. 2008), they are usually small molecules, such as methane, alkanes, formic acid, and acetate. In addition, while organic compounds could accumulate in Martian soil via volcanic degassing, they are expected to degrade during long-term exposure under relatively oxidizing conditions and by ultraviolet radiation on the red planet (Oró and Holzer 1979; Stoker and Bullock 1997; Shkrob et al. 2010; Poch et al. 2013), because most volcanic activities took place about 3 Ga ago (Ehlmann et al. 2011). For this reason, a hydrothermal origin is not favorable for the kerogen-like organic matter.

Another possible abiogenic source of the organic matter is IDPs and carbonaceous chondrites, which hit the surface of Mars (Flynn 1996; Becker et al. 1999). IDPs contain abundant organic matter, but it is commonly D- and/or ^{15}N-enriched (Messenger 2000; Aléon et al. 2001, 2003; Floss et al. 2006; Duprat et al. 2010). Aléon et al. (2001) have recognized three endmembers of OM in IDPs; two of them, referred to as OM2 and OM3, are extremely D-enriched (up to 8000‰) and the third, OM1, has δD of 630‰. Furthermore, all three endmembers are ^{15}N-enriched

Table 5. Isotopic compositions and elemental ratios of C and N of the organic matter.

Sample ID	N/C[a]	$\delta^{15}N$[b]	SE	K_{corr}	$\delta^{13}C_{raw}$	SE	$\delta^{13}C_{PHD}$	$\delta^{13}C_{QSA}$	$\delta^{13}C$	SE*	IMF
Graphite-1a	2.81E-4	−38.9	37.8	0.041	−40.2	1.0	−40.2	−73.7	−35.1	3.1	
Graphite-1a	2.68E-4	−59.0	38.5	0.041	−37.3	1.0	−37.4	−70.9	−32.3	3.1	
Graphite-1a	3.29E-4	−24.7	34.2	0.040	−37.7	1.0	−37.7	−70.3	−31.8	3.0	
Graphite-1a	2.09E-4	−96.0	42.9	0.040	−37.8	0.9	−37.9	−70.5	−32.0	3.1	
Graphite-1a	2.61E-4	−83.4	37.2	0.041	−38.6	1.0	−38.7	−72.2	−33.6	3.2	
Graphite-1a	3.51E-4	−31.6	35.1	0.040	−39.9	1.0	−39.9	−72.5	−34.0	3.0	
Graphite-1a	2.53E-4	−12.1	38.3	0.040	−39.3	1.0	−39.3	−71.9	−33.4	3.4	
Average	*2.79E-4*	*−49.4*						*−71.7*	*−33.1*		*−38.6*
SD	*4.77E-5*	*31.2*						*1.2*	*1.2*		
58C3	1.61E-2	8.3	5.6	0.029	−48.0	1.1	−48.0	−71.7	−33.1	2.9	−38.6
57C3	1.47E-2	7.3	7.4	0.026	−33.3	1.5	−33.3	−54.5	−15.9	3.2	−38.6
Graphite-1b	8.18E-5	−12.8	74.5	0.043	−41.9	1.1	−41.9	−77.0	−34.6	3.4	
Graphite-1b	7.89E-5	47.7	80.9	0.042	−40.1	1.0	−40.0	−74.3	−31.9	3.3	
Graphite-1b	8.00E-5	179.1	73.0	0.043	−40.2	1.0	−40.1	−75.2	−32.8	3.3	
Average	*8.02E-5*	*71.3*						*−75.5*	*−33.1*		*−42.3*
SD	*1.49E-6*	*98.1*						*1.4*	*1.4*		
55C2a	3.48E-3	17.3	11.8	0.046	−20.5	0.9	−20.3	−57.8	−15.5	3.1	−42.3
55C3	6.69E-3	−1.1	8.1	0.037	−30.8	1.2	−30.6	−60.8	−18.4	3.3	−42.3
55C4	7.49E-3	−1.1	9.3	0.035	−26.9	1.2	−26.6	−55.2	−12.8	3.3	−42.3
55C1	1.47E-2	5.8	6.5	0.035	−32.3	1.1	−32.0	−60.6	−18.2	3.2	−42.3
58C4	1.10E-2	16.7	7.1	0.036	−32.5	1.2	−32.2	−61.6	−19.2	3.3	−42.3
58C5	8.83E-3	1.9	9.1	0.031	−39.4	1.3	−39.0	−64.3	−22.0	3.4	−42.3
58C1	5.62E-3	3.8	9.3	0.043	−28.0	1.0	−27.6	−62.7	−20.3	3.2	−42.3
58C7	1.34E-2	12.4	9.1	0.042	−27.8	1.6	−27.3	−61.6	−19.2	3.6	−42.3
58C6	8.56E-3	−12.9	9.0	0.031	−41.2	1.4	−40.7	−66.0	−23.7	3.4	−42.3
58C2	2.27E-2	−3.3	5.8	0.027	−45.7	1.3	−45.1	−67.1	−24.8	3.3	−42.3
56Cb	6.96E-3	1.5	8.0	0.042	−34.8	1.2	−34.2	−68.5	−26.1	3.3	−42.3
Average	*1.08E-2*	*4.4*							*−20.7*		
SD	*5.31E-3*	*8.4*							*5.3*		

[a]N/C ratios were calibrated with a RSF of 0.13, which was determined with the coal reference. The analytical uncertainties of N/C ratios are dominated by heterogeneity of the coal reference (9.5%).

[b]$\delta^{15}N$ values were calibrated for matrix effect with an IMF of $-2.1 \pm 5.6‰$, which was determined with the coal reference, here IMF $\approx \delta^{15}N_{meas} - \delta^{15}N_{true}$ and $\delta^{15}N_{true} = 2.97 \pm 0.19‰$.

$\delta^{15}N = (({}^{12}C^{15}N/{}^{12}C^{14}N)_{sample}/({}^{12}C^{15}N/{}^{12}C^{14}N)_{standard} - 1) \times 1000‰$, here $({}^{15}N/{}^{14}N)_{standard} = 0.003673$ (air). $\delta^{13}C = (({}^{13}C/{}^{12}C)_{sample}/({}^{13}C/{}^{12}C)_{VPDB} - 1) \times 1000‰$, here $({}^{13}C/{}^{12}C)_{VPDB} = 0.0112372$.

K_{corr} = the secondary ions ejected per primary ion.

$\delta^{13}C_{Raw}$ = Raw data. $\delta^{13}C_{PHD}$ = PHD_{max} corrected. $\delta^{13}C_{QSA}$ = QSA corrected using parameter K_{corr}.

$\delta^{13}C_{QSA} = \delta^{13}C_{PHD} - (0.816 \times K_{corr}) \times 1000‰$.

$\delta^{13}C$ = final correction for IMF, with $\delta^{13}C_{true} \approx \delta^{13}C_{QSA}$-IMF. The measurements were carried out in two separate sessions with different IMF values.

Standard error (SE) is statistical uncertainty.

SE* = The combined analytical error includes counting uncertainty and correction uncertainties of PHD, QSA, and IMF.

($\delta^{15}N$ 200–400‰) (Aléon et al. 2003). Hence, the very heavy H and N isotopic compositions of IDPs are not a likely source of the organic matter in Tissint.

Carbonaceous chondrites also contain high abundances of organic matter, up to approximately 2 wt%, the bulk of which is kerogen or insoluble organic matter (IOM) (Pizzarello et al. 2006; Alexander et al. 2010). The δD and $\delta^{13}C$ data of the organic matter in Tissint are plotted in Fig. 8, and are compared with IOM, organic acids, and various hydrocarbons from the Murchison (CM2) meteorite, as well as IOM from various other groups of carbonaceous chondrites. Some of the less ^{13}C-depleted organic matter in Tissint overlaps the IOM from Murchison and other CM group meteorites, as well as the CV group and the ungrouped Tagish Lake carbonaceous chondrite, but is distinguished from IOM in the CR and CO groups. It is also distinctly lighter in C isotopes than all extractible organic compounds from Murchison. Figure 7 compares elemental ratios of the organic matter in Tissint with IOM of various groups of carbonaceous chondrites reported by Alexander et al. (2007). The organic matter in Tissint overlaps the IOM from CV, CO, and thermally metamorphosed CMs, but has lower

Table 6. Isotopic compositions of H and H/C ratios of the organic matter.

Sample ID	H/C*	δD	SE
58C3		882.6	13.0
57C3		1079.9	10.3
55C2a	0.324	364.4	11.7
55C3	0.287	323.8	9.9
55C4	0.106	424.4	13.2
55C1	0.399	790.7	11.1
58C4	0.344	358.4	9.1
58C5	0.460	−50.6	10.0
58C1	0.360	−4.5	13.5
58C7	0.137	357.7	16.4
58C6	0.352	6.7	14.6
58C2	0.308	−31.4	15.6
56Cb	0.146	1183.1	15.1
Average	*0.293*	*437*	
SD	*0.115*	*424*	
Graphite-1	0.036	−151.2	18.3
Graphite-1	0.043	−155.2	18.4
Average	*0.040*	*−153.2*	
SD	*0.005*	*2.9*	
Coal	0.707	−111.7	11.0
Coal	0.852	−158.4	10.7
Coal	0.936	−168.4	14.1
Coal	0.681	−137.9	13.0
Coal	0.509	−145.4	10.3
Coal	0.668	−160.3	10.3
Average	*0.726*	*−147.0*	
SD	*0.150*	*20.5*	

H/C* ratios were calibrated with a RSF of 6.7, which was determined from the coal reference. The analytical uncertainties are dominated by the heterogeneity of the reference (approximately 21%).

$\delta D = ((D/H)_{sample}/(D/H)_{SMOW} - 1) \times 1000‰$, here $(D/H)_{SMOW} = 1.55 \times 10^{-4}$.

The δD values of the samples have been corrected for IMF (−128‰) using the coal reference with δD of −147 ± 1.2‰. $\delta D_{true} \approx \delta D_{meas}$-IMF; The standard error (SE) is statistical uncertainty; SD = standard deviation of analyses.

Two grains (58C3 and 57C3) were measured without counting C in the first analysis session.

H/C, N/C, and O/C ratios than CM, CR, and CI groups and the ungrouped Tagish Lake meteorite. The lower concentrations of H, N, and O in IOM from the heated CMs than from that in the primitive CMs indicate chemical variation related to thermal metamorphism. This may explain the difference between the organic matter in Tissint and the IOM from primitive CMs. Based on the overall similarities in isotopic and elemental compositions, the CV and CM groups would be the most likely sources for the organic matter in Tissint.

However, regardless of these similarities, there are two main problems with an external source for the organic matter in Tissint. The first is how to extract IOM from meteorites and/or IDPs that hit the surface of Mars, and then deposit it in fractures in Tissint? IOM in meteorites occurs intermingled with the fine-grained matrix, and it would have been highly diluted and mixed with Martian soil when meteorites and IDPs impact the surface of Mars. IOM can be concentrated in the laboratory only through dissolving all silicate minerals using HF and other strong acids. It would be much more difficult to extract IOM from the Martian soil, because it is present only in very low concentrations, as determined by Mars Rovers (Biemann et al. 1976; Leshin et al. 2013; Ming et al. 2014). The second problem is that about half of the organic carbon grains we analyzed have more negative $\delta^{13}C$ (up to −33‰) than the ranges of IOM from CMs and CVs (Fig. 8). The more ^{13}C-depleted compositions would not be explained by degradation due to UV radiation or oxidization. UV radiation of Murchison carbonaceous chondrite under conditions similar to those expected at the Martian surface releases methane that is ^{13}C-depleted ($\delta^{13}C = -30‰ \sim -60‰$) relative to the original organic compounds (Keppler et al. 2012). Therefore, this process would enhance the $\delta^{13}C$ values of the residual organic matter, in contrast to our observations. In summary, therefore, although IOM from CMs and CVs could theoretically be the source of the organic matter in Tissint, the lighter C isotopic compositions of the latter and, especially, the lack of a specific process for extracting trace IOM from the Martian soil remain unsolved problems.

Evidence for a Biogenic Origin of the Organic Matter

An alternative source for the organic matter in Tissint is past biotic activities in the subsurface of Mars, which was then carried by subsurface fluids that infiltrated factures in the Tissint host rock.

A biogenic origin of the organic matter is supported by the significantly low $\delta^{13}C$ values measured with NanoSIMS. Figure 9 shows the $\delta^{13}C$ values of the organic matter, compared with the C isotopic compositions of Martian atmospheric CO_2 and carbonates in Martian meteorites. The difference between the organic matter and the Martian atmospheric CO_2 is at least −10‰ to −30‰ (an average of −18‰) relative to a value of −2.5 ± 4.2‰ determined by the Phoenix lander (Niles et al. 2010), and is much larger than new measurements by the Curiosity Mars rover (45 ± 12‰, Mahaffy et al. 2013; +46 ± 4‰, Webster et al. 2013). The magnitude and direction of the C isotope fractionations observed in Tissint organic matter are comparable to those produced by biotic activities on Earth (Fig. 9).

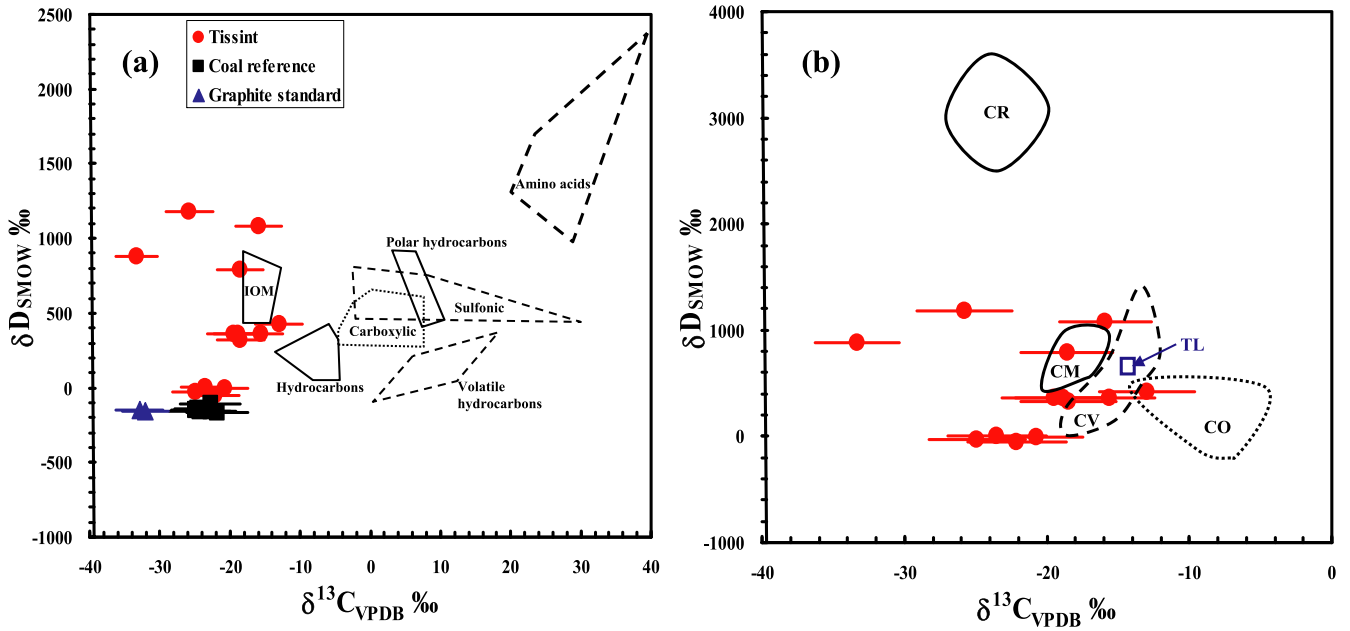

Fig. 8. Comparison of δD and $\delta^{13}C$ values of organic matter in Tissint and carbonaceous chondrites. a) Organic matter from Tissint has lighter C than various soluble organic molecules (including amino acids, polar hydrocarbons, sulfonic acids, carboxylic acids, volatile hydrocarbons, and hydrocarbons) from Murchison, but overlaps with IOM from the same meteorite. b) H and C isotopes of the organic matter from Tissint overlap with bulk IOM from CM and CV groups and the ungrouped Tagish Lake (TL) carbonaceous chondrite, but differ from that of CR and CO groups. The Murchison IOM and various soluble organic compounds are from Martins (2011), and the ranges of bulk IOM from various groups of carbonaceous chondrites are from Alexander et al. (2007).

The δD values of the organic matter in Tissint vary from +324‰ to +1183‰, except for four analyses with nearly normal H isotopes. These δD values are significantly lower than the Martian atmospheric water (approximately 4200‰, Watson et al. 1994; 6034 ± 72‰, Hu et al. 2014). However, lower δD values have also been reported in the Martian crustal regolith NWA 7034 (+46.3 ± 8.6‰, ranging between −100‰ and +327‰), which contains a bulk water content of 6190 ± 620 ppm (Agee et al. 2013). Although Martian atmospheric water is highly D-enriched, there has probably not been liquid water on the surface of Mars since the Amazonian period, due to the cold and arid conditions that have probably prevailed on the surface over the last 3 billion years (Ehlmann et al. 2011). Instead, underground water could be produced via melting of subsurface ice through the emplacement of magmas (Hu et al. 2014), which mixed with isotopically normal water from the Martian mantle (Leshin 2000; Gillet et al. 2002; Usui et al. 2012) and resulted in a wide range of δD. The $\delta^{15}N$ values of the organic carbon are between −12.9‰ and +17.3‰ with an average of 4.4 ± 8.4‰, similar to the N reservoir of the Martian crust (−30 to +40‰) (Mathew et al. 2003; Mohapatra et al. 2009) rather than the Martian atmosphere (approximately 600‰) (Jakosky and Phillips 2001).

CONCLUSIONS

Two petrographic settings of kerogen-like organic matter were observed in the newly fallen Tissint Martian meteorite. Most of the organic matter fills fractures in olivine and pyroxene, but some also occurs entrained in shock-melt veins. The presence of the organic matter encapsulated in the shock-melt veins strongly suggests its formation predating the impact event, a robust evidence for a Martian origin and not terrestrial contamination. This is supported by transformation of a part of the organic matter in the shock-melt veins into diamond, as well as by the high D-enrichments (δD up to 1183‰) of the grains. The organic matter in the fractures can be interpreted as the result of deposition from organic-rich fluids near the Martian surface. In addition, significant ^{13}C-depletions ($\delta^{13}C$ = −12.8‰ to −33.1‰), relative to Martian atmospheric CO_2, are consistent with a biogenic origin. The presence of organic matter in the fractures in Tissint is difficult to explain through magmatic precipitation of reduced carbon components during igneous crystallization. In addition, although an abiogenic origin via meteoritic delivery cannot be completely excluded because of overlapping chemical and isotopic compositions, it remains unclear how to extract trace amounts of insoluble organic matter from

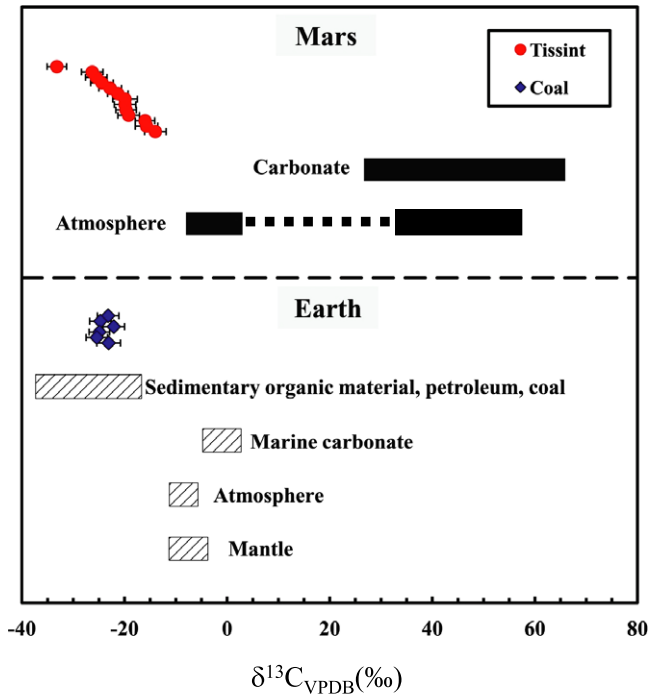

Fig. 9. Carbon isotopic compositions in Martian and terrestrial reservoirs. The organic matter in Tissint is significantly lighter than the C isotopic compositions of the Martian atmospheric CO_2 measured by the Phoenix lander (-2.5 ± 4.3‰) (Niles et al. 2010) and by the Curiosity Mars rover (45 ± 12‰, Mahaffy et al. 2013; $+46 \pm 4$‰, Webster et al. 2013), as well as ALH 84001 carbonate (Niles et al. 2005). This difference is comparable to that between biogenic and abiogenic carbonaceous materials on Earth (Hoefs 2009). Coal is the working reference.

the Martian soil. We thus favor a biogenic origin for the organic matter in Tissint.

Acknowledgments—The constructive reviews by three anonymous reviewers, the AE C. Floss, and the Editor T. Jull are very helpful to improve the manuscript. We thank Gangjian Wei and Lianjun Feng for the isotopic measurements of the graphite standards and the coal working reference. This work was supported by Chinese Academy of Science and National Science Foundation of China (40830421, 41221002, 41430105).

Editorial Handling—Dr. Dr. A. J. Timothy Jull

REFERENCES

Agee C. B., Wilson N. V., McCubbin F. M., Ziegler K., Polyak V. J., Sharp Z. D., Asmerom Y., Nunn M. H., Shaheen R., Thiemens M. H., Steele A., Fogel M. L., Bowden R., Glamoclija M., Zhang Z., and Elardo S. M. 2013. Unique meteorite from early Amazonian Mars: Water-rich basaltic breccia Northwest Africa 7034. *Science* 339:780–785.

Aléon J., Engrand C., Robert F., and Chaussidon M. 2001. Clues to the origin of interplanetary dust particles from the isotopic study of their hydrogen-bearing phases. *Geochimica et Cosmochimica Acta* 65:4399–4412.

Aléon J., Robert F., Chaussidon M., and Marty B. 2003. Nitrogen isotopic composition of macromolecular organic matter in interplanetary dust particles. *Geochimica et Cosmochimica Acta* 67:3773–3783.

Alexander C. M. O'D., Fogel M., Yabuta H., and Cody G. D. 2007. The origin and evolution of chondrites recorded in the elemental and isotopic compositions of their macromolecular organic matter. *Geochimica et Cosmochimica Acta* 71:4380–4403.

Alexander C. M. O'D., Newsome S. D., Fogel M. L., Nittler L. R., Busemann H., and Cody G. D. 2010. Deuterium enrichments in chondritic macromolecular material–Implications for the origin and evolution of organics, water and asteroids. *Geochimica et Cosmochimica Acta* 74:4417–4437.

Becker L., Popp B., Rust T., and Bada J. L. 1999. The origin of organic matter in the Martian meteorite ALH 84001. *Advances in Space Research* 24:477–488.

Biemann K., Oro J., Toulmin P., Orgel L. E., Nier A. O., Anderson D. M., Simmonds P. G., Flory D., Diaz A. V., Rushneck D. R., and Biller J. A. 1976. Search for organic and volatile inorganic compounds in two surface samples from the Chryse Planitia region of Mars. *Science* 194:72–76.

Campbell J. L., Gellert R., Lee M., Mallett C. L., Maxwell J. A., and O'Meara J. M. 2008. Quantitative in situ determination of hydration of bright high-sulfate Martian soils. *Journal of Geophysical Research* 113:E06S11.

Chennaoui Aoudjehane H., Avice G., Barrat J. A., Boudouma O., Chen G., Duke M. J. M., Franchi I. A., Gattacceca J., Grady M. M., Greenwood R. C., Herd C. D. K., Hewins R., Jambon A., Marty B., Rochette P., Smith C. L., Sautter V., Verchovsky A., Weber P., and Zanda B. 2012. Tissint Martian meteorite: A fresh look at the interior, surface, and atmosphere of Mars. *Science* 338:785–788.

Duprat J., Dobrica E., Engrand C., Aleon J., Marrocchi Y., Mostefaoui S., Meibom A., Leroux H., Rouzaud J. N., Gounelle M., and Robert F. 2010. Extreme deuterium excesses in ultracarbonaceous micrometeorites from central Antarctic snow. *Science* 328:742–745.

Ehlmann B. L., Mustard J. F., Murchie S. L., Bibring J.-P., Meunier A., Fraeman A. A., and Langevin Y. 2011. Subsurface water and clay mineral formation during the early history of Mars. *Nature* 479:53–60.

El Goresy A., Gillet P., Miyahara M., Ohtani E., Ozawa S., Beck P., and Montagnac G. 2013a. Shock-induced deformation of Shergottites: Shock-pressures and perturbations of magmatic ages on Mars. *Geochimica et Cosmochimica Acta* 101:233–262.

El Goresy A., Gillet P., Miyahara M., Ohtani E., Ozawa S., Lin Y., Feng L., and Escerig S. 2013b. Multiple shock events and diamond formation on Mars (abstract #1037). 44th Lunar and Planetary Science Conference. CD-ROM.

Floss C., Stadermann F. J., Bradley J. P., Dai Z. R., Bajt S., Graham G., and Lea A. S. 2006. Identification of isotopically primitive interplanetary dust particles: A NanoSIMS isotopic imaging study. *Geochimica et Cosmochimica Acta* 70:2371–2399.

Flynn G. 1996. The delivery of organic matter from asteroids and comets to the early surface of Mars. *Earth, Moon, and Planets* 72:469–474.

Formisano V., Atreya S., Encrenaz T., Ignatiev N., and Giuranna M. 2004. Detection of methane in the atmosphere of Mars. *Science* 306:1758–1761.

Foustoukos D. I. and Seyfried W. E. 2004. Hydrocarbons in hydrothermal vent fluids: The role of chromium-bearing catalysts. *Science* 304:1002–1005.

Gillet P., Barrat J. A., Deloule E., Wadhwa M., Jambon A., Sautter V., Devouard B., Neuville D., Benzerara K., and Lesourd M. 2002. Aqueous alteration in the Northwest Africa 817 (NWA 817) Martian meteorite. *Earth and Planetary Science Letters* 203:431–444.

Grady M. M., Verchovsky A. B., and Wright I. P. 2004. Magmatic carbon in Martian meteorites: Attempts to constrain the carbon cycle on Mars. *International Journal of Astrobiology* 3:117–124.

Hecht M. H., Kounaves S. P., Quinn R. C., West S. J., Young S. M. M., Ming D. W., Catling D. C., Clark B. C., Boynton W. V., Hoffman J., DeFlores L. P., Gospodinova K., Kapit J., and Smith P. H. 2009. Detection of perchlorate and the soluble chemistry of Martian soil at the Phoenix Lander site. *Science* 325:64–67.

Hoefs J. 2009. *Stable isotope geochemistry*. Berlin: Springer-Verlag. 285 p.

Hu S., Lin Y. T., Zhang J. C., Hao J. L., Feng L., Xu L., Yang W., and Yang J. 2014. Hydrogen isotope evidence for near-surface hydrothermal activity on Mars in recent past. *Geochimica et Cosmochimica Acta* 140:321–333.

Irving A. J., Kuehner S. M., Tanaka R., Herd C. D. K., Chen G., and Lapen T. J. 2012. The Tissint depleted permafic olivine-phyric shergottite: Petrologic, elemental and isotopic characterization of a recent fall in Morocco (abstract #2510). 43rd Lunar and Planetary Science Conference. CD-ROM.

Jakosky B. M. and Phillips R. J. 2001. Mars' volatile and climate history. *Nature* 412:237–244.

Jia G. D., Peng P. A., Zhao Q. H., and Jian Z. M. 2003. Changes in terrestrial ecosystem since 30 Ma in East Asia: Stable isotope evidence from black carbon in the South China Sea. *Geology* 31:1093–1096.

Keppler F., Vigano I., McLeod A., Ott U., Fruchtl M., and Rockmann T. 2012. Ultraviolet-radiation-induced methane emissions from meteorites and the Martian atmosphere. *Nature* 486:93–96.

Kerr R. A. 2012. Question of Martian methane is still up in the air. *Science* 338:733.

Lepland A., Van Zuilen M. A., and Philippot P. 2010. Fluid-deposited graphite and its geobiological implications in early Archean gneiss from Akilia, Greenland. *Geobiology* 9:2–9.

Leshin L. A. 2000. Insights into Martian water reservoirs from analyses of Martian meteorite QUE 94201. *Geophysical Research Letters* 27:2017–2020.

Leshin L. A., Mahaffy P. R., Webster C. R., Cabane M., Coll P., Conrad P. G., Archer P. D., Atreya S. K., Brunner A. E., Buch A., Eigenbrode J. L., Flesch G. J., Franz H. B., Freissinet C., Glavin D. P., McAdam A. C., Miller K. E., Ming D. W., Morris R. V., Navarro-González R., Niles P. B., Owen T., Pepin R. O., Squyres S., Steele A., Stern J. C., Summons R. E., Sumner D. Y., Sutter B., Szopa C., Teinturier S., Trainer M. G., Wray J. J., and Grotzinger J. P., and the MSL Science Team. 2013. Volatile, isotope, and organic analysis of Martian Fines with the Mars Curiosity rover. *Science* 341:1238937-1–1238937-9.

Li L., Ren D., Du X., Wu P., Chen L., Ma Z., and Wang Q. 2003. *Analytical method of element for carbon, hydrogen and oxygen in rock organics*: General Administration of Quality Supervision, Inspection and Quarantine of the People's Republic of China. GB/T 19143-2003 p. In Chinese.

Lin Y. T., Hu S., Feng L., Zhang J. C., Hao J. L., and Xu L. 2012. Petrography and shock metamorphism of the Tissint olivine-phyric shergottite (abstract). *Meteoritics & Planetary Science* 48:5131.

Lin Y., El Goresy A., Hu S., Zhang J., Gillet P., Xu Y., Hao J., Miyahara M., Ouyang Z., Ohtani E., Xu L., Yang W., Feng L., Zhao X., Yang J., and Ozawa S. 2013a. NanoSIMS analysis of organic carbon from Mars: Evidence for a biogenetic origin (abstract #1476). 44th Lunar and Planetary Science Conference. CD-ROM.

Lin Y., El Goresy A., Hu S., Zhang J., Gillet P., Xu Y., Hao J., Miyahara M., Ouyang Z., Ohtani E., Xu L., Yang W., Feng L., Zhao X., Yang J., and Ozawa S. 2013b. Organic carbon from the Tissint Martian meteorite: Hints for biogenic origin (abstract #1614). Goldschmidt Conference.

Lin Y., El Goresy A., Hu S., Zhang J., Gillet P., Xu Y., Hao J., Miyahara M., Ouyang Z., Ohtani E., Xu L., Yang W., Feng L., Zhao X., Yang J., and Ozawa S. 2013c. Underground organic-rich fluids on Mars: Biotic vs abiotic processes (abstract #5096). *Meteoritics & Planetary Science* 48.

Lollar B. S., Lacrampe-Couloume G., Voglesonger K., Onstott T. C., Pratt L. M., and Slater G. F. 2008. Isotopic signatures of CH_4 and higher hydrocarbon gases from Precambrian Shield sites: A model for abiogenic polymerization of hydrocarbons. *Geochimica et Cosmochimica Acta* 72:4778–4795.

Mahaffy P. R., Webster C. R., Atreya S. K., Franz H., Wong M., Conrad P. G., Harpold D., Jones J. J., Leshin L. A., Manning H., Owen T., Pepin R. O., Squyres S., and Trainer M., and the MSL Science Team. 2013. Abundance and isotopic composition of gases in the Martian atmosphere from the Curiosity rover. *Science* 341:263–266.

Martins Z. 2011. Organic chemistry of carbonaceous meteorites. *Elements* 7:35–40.

Mathew K. J., Marty B., Marti K., and Zimmermann L. 2003. Volatiles (nitrogen, noble gases) in recently discovered SNC meteorites, extinct radioactivities and evolution. *Earth and Planetary Science Letters* 214:27–42.

McCollom T. M., Lollar B. S., Lacrampe-Couloume G., and Seewald J. S. 2010. The influence of carbon source on abiotic organic synthesis and carbon isotope fractionation under hydrothermal conditions. *Geochimica et Cosmochimica Acta* 74:2717–2740.

Messenger S. 2000. Identification of molecular-cloud material in interplanetary dust particles. *Nature* 404:968–971.

Ming D. W., Archer P. D., Glavin D. P., Eigenbrode J. L., Franz H. B., Sutter B., Brunner A. E., Stern J. C., Freissinet C., McAdam A. C., Mahaffy P. R., Cabane M., Coll P., Campbell J. L., Atreya S. K., Niles P. B., Bell J. F., Bish D. L., Brinckerhoff W. B., Buch A., Conrad P. G., Des Marais D. J., Ehlmann B. L., Fairén A. G., Farley K., Flesch G. J., Francois P., Gellert R., Grant J. A., Grotzinger J. P., Gupta S., Herkenhoff K. E., Hurowitz J. A., Leshin L. A., Lewis K. W., McLennan S. M., Miller K. E., Moersch J., Morris R. V., Navarro-González R., Pavlov A. A., Perrett G. M., Pradler I., Squyres S. W., Summons R. E., Steele A., Stolper E. M., Sumner D. Y., Szopa C., Teinturier S., Trainer M. G., Treiman A. H., Vaniman D.

T., Vasavada A. R., Webster C. R., Wray J. J., and Yingst R. A., and the MSL Science Team. 2014. Volatile and organic compositions of sedimentary rocks in Yellowknife Bay, Gale Crater, Mars. *Science* 343:1245267-1–1245267-9.

Mohapatra R. K., Schwenzer S. P., Herrmann S., Murty S. V. S., Ott U., and Gilmour J. D. 2009. Noble gases and nitrogen in Martian meteorites Dar al Gani 476, Sayh al Uhaymir 005 and Lewis Cliff 88516: EFA and extra neon. *Geochimica et Cosmochimica Acta* 73:1505–1522.

Niles P. B., Leshin L. A., and Guan Y. 2005. Microscale carbon isotope variability in ALH 84001 carbonates and a discussion of possible formation environments. *Geochimica et Cosmochimica Acta* 69:2931–2944.

Niles P. B., Boynton W. V., Hoffman J. H., Ming D. W., and Hamara D. 2010. Stable isotope measurements of Martian atmospheric CO_2 at the Phoenix landing site. *Science* 329:1334–1337.

Oró J. and Holzer G. 1979. The photolytic degradation and oxidation of organic compounds under simulated Martian conditions. *Journal of Molecular Evolution* 14:153–160.

Osterloo M. M., Hamilton V. E., Bandfield J. L., Glotch T. D., Baldridge A. M., Christensen P. R., Tornabene L. L., and Anderson F. S. 2008. Chloride-bearing materials in the southern highlands of Mars. *Science* 319:1651–1654.

Pizzarello S., Cooper G. W., and Flynn G. J. 2006. The nature and distribution of the organic material in carbonaceous chondrites and interplanetary dust particles. In *Meteorites and the early solar system II*, edited by Lauretta D. S. and McSween H. Y. Jr. Tucson, Arizona: The University of Arizona Press. pp. 625–651.

Poch O., Noblet A., Stalport F., Correia J. J., Grand N., Szopa C., and Coll P. 2013. Chemical evolution of organic molecules under Mars-like UV radiation conditions simulated in the laboratory with the "Mars organic molecule irradiation and evolution" (MOMIE) setup. *Planetary and Space Science* 85:188–197.

Proskurowski G., Lilley M. D., Seewald J. S., Früh-Green G. L., Olson E. J., Lupton J. E., Sylva S. P., and Kelley D. S. 2008. Abiogenic hydrocarbon production at Lost City hydrothermal field. *Science* 319:604–607.

Schmidt M. E., Ruff S. W., McCoy T. J., Farrand W. H., Johnson J. R., Gellert R., Ming D. W., Morris R. V., Cabrol N., Lewis K. W., and Schroeder C. 2008. Hydrothermal origin of halogens at Home Plate, Gusev Crater. *Journal of Geophysical Research* 113:E06S12.

Schwab V., Spangenberg J. E., and Grimalt J. O. 2005. Chemical and carbon isotopic evolution of hydrocarbons during prograde metamorphism from 100 degrees C to 550 degrees C: Case study in the Liassic black shale formation of Central Swiss Alps. *Geochimica et Cosmochimica Acta* 69:1825–1840.

Shkrob I. A., Chemerisov S. D., and Marin T. W. 2010. Photocatalytic decomposition of carboxylated molecules on light-exposed Martian regolith and its relation to methane production on Mars. *Astrobiology* 10:425–436.

Slodzian G. 2004. Challenges in localized high precision isotope analysis by SIMS. *Applied Surface Science* 231–232:3–12.

Slodzian G., Hillion F., Stadermann F. J., and Zinner E. 2004. QSA influences on isotopic ratio measurements. *Applied Surface Science* 231:874–877.

Squyres S. W., Arvidson R. E., Bell J. F., Brückner J., Cabrol N. A., Calvin W., Carr M. H., Christensen P. R., Clark B. C., Crumpler L., Marais D. J. D., d'Uston C., Economou T., Farmer J., Farrand W., Folkner W., Golombek M., Gorevan S., Grant J. A., Greeley R., Grotzinger J., Haskin L., Herkenhoff K. E., Hviid S., Johnson J., Klingelhöfer G., Knoll A. H., Landis G., Lemmon M., Li R., Madsen M. B., Malin M. C., McLennan S. M., McSween H. Y., Ming D. W., Moersch J., Morris R. V., Parker T., Rice J. W., Richter L., Rieder R., Sims M., Smith M., Smith P., Soderblom L. A., Sullivan R., Wänke H., Wdowiak T., Wolff M., and Yen A. 2004. The Opportunity Rover's Athena Science Investigation at Meridiani Planum, Mars. *Science* 306:1698–1703.

Steele A., McCubbin F. M., Fries M., Kater L., Boctor N. Z., Fogel M. L., Conrad P. G., Glamoclija M., Spencer M., Morrow A. L., Hammond M. R., Zare R. N., Vicenzi E. P., Siljeström S., Bowden R., Herd C. D. K., Mysen B. O., Shirey S. B., Amundsen H. E. F., Treiman A. H., Bullock E. S., and Jull A. J. T. 2012. A reduced organic carbon component in Martian basalts. *Science* 337:212–215.

Stoker C. R. and Bullock M. A. 1997. Organic degradation under simulated Martian conditions. *Journal of Geophysical Research: Planets* 102:10,881–10,888.

Usui T., Alexander C. M. O'D., Wang J., Simon J. I., and Jones J. H. 2012. Origin of water and mantle-crust interactions on Mars inferred from hydrogen isotopes and volatile element abundances of olivine-hosted melt inclusions of primitive shergottites. *Earth and Planetary Science Letters* 357–358:119–129.

Watson L. L., Hutcheon I. D., Epstein S., and Stolper E. M. 1994. Water on Mars: Clues from deuterium/hydrogen and water contents of hydrous phases in SNC meteorites. *Science* 265:86–90.

Webster C. R., Mahaffy P. R., Flesch G. J., Niles P. B., Jones J. H., Leshin L. A., Atreya S. K., Stern J. C., Christensen L. E., Owen T., Franz H., Pepin R. O., and Steele A., and the MSL Science Team. 2013. Isotope ratios of H, C, and O in CO_2 and H_2O of the Martian atmosphere. *Science* 341:260–263.

Wopenka B. and Pasteris J. D. 1993. Structural characterization of kerogens to granulite-facies graphite: Applicability of Raman microprobe spectroscopy. *American Mineralogist* 78:533–557.

Zhang J., Lin Y., Yang W., Shen W., Hao J., Hu S., and Cao M. 2014. Improved precision and spatial resolution of sulfur isotope analysis using NanoSIMS. *Journal of Analytical Atomic Spectrometry* 29:1934–1943.